JGR Atmospheres

RESEARCH ARTICLE
10.1029/2018JD029986

Weather Radar Insights Into the Turbulent Dynamics of a Wildfire-Triggered Supercell Thunderstorm

Alex Terrasson[1,2], Nicholas McCarthy[3], Andrew Dowdy[4], Harald Richter[4], Hamish McGowan[3], and Adrien Guyot[2,5]

[1]Laboratoire de Mécanique des Fluides et d'Acoustique, Ecole Centrale de Lyon, Ecully, France, [2]School of Civil Engineering, University of Queensland, Brisbane, Queensland, Australia, [3]Atmospheric Observations Research Group, School of Earth and Environmental Sciences, University of Queensland, Brisbane, Queensland, Australia, [4]Bureau of Meteorology, Melbourne, Victoria, Australia, [5]Department of Civil Engineering, Monash University, Melbourne, Victoria, Australia

Abstract Understanding wildfire-atmosphere interactions is key to improved accuracy of predictions of wildfire behavior. This is needed for improved preparedness to mitigate loss of life and property during wildfire events, particularly for situations with strong fire-atmosphere coupling. Here we present observations from the passage of a cold front over the Sir Ivan Dougherty wildfire on February 2017 in eastern Australia. We demonstrate that an increase in near-surface atmosphere moisture associated with the cold front, when combined with changes in fire behavior at that time, led to reduced thermodynamic stability that helped to trigger a thunderstorm. This fire-trigged supercell thunderstorm produced lightning, while radar observations identified a mesocyclonic circulation within the pyrocumulonimbus, similar to a supercell thunderstorm. Results highlight the need to monitor the thermodynamic properties of air masses approaching wildfires and the rapid evolution of pyrocumulonimbus, which may develop mesocyclone characteristics. Weather radar offers the most effective capability to achieve such insights.

Plain Language Summary Here we present observations of the behavior of a wildfire and associated meteorology over a large wildfire in eastern Australia. By analyzing weather radar data and meteorological data from close proximity to the fire, we show that an increase in atmospheric moisture due to the passage of a cold front over the fire ground, combined with changes in fire behavior at that time, was sufficient to trigger development of a wildfire-induced thunderstorm. This fire-generated storm produced lightning and began to rotate similar to a supercell thunderstorm. We conclude by highlighting the capability of weather radar in combination with standard meteorological observations to provide valuable insight to fire-atmosphere coupling. These observations are essential to build understanding of extreme wildfire events for enabling improved prediction of their behavior to reduce loss of life and property in firestorms.

Key Points:
- Genesis, growth, and decay of a pyroconvective thunderstorm are studied combining ground weather radar, atmospheric profiling, and micrometeorological observations
- Observations of fire-atmosphere interactions enable quantification of pyroconvective thunderstorm turbulence and kilometer-scale vortices
- An "optimal" window of conditions is identified for a fire to trigger thunderstorm genesis and generate lightning that can ignite new fires

Supporting Information:
- Supporting Information SI

Correspondence to:
A. Guyot,
adrien.guyot@monash.edu

Citation:
Terrasson, A., McCarthy, N., Dowdy, A., Richter, H., McGowan, H., & Guyot, A. (2019). Weather radar insights into the turbulent dynamics of a wildfire-triggered supercell thunderstorm. *Journal of Geophysical Research: Atmospheres*, *124*, 8645–8658. https://doi.org/10.1029/2018JD029986

Received 14 NOV 2018
Accepted 11 JUL 2019
Accepted article online 16 JUL 2019
Published online 2 AUG 2019

Author Contributions:
Conceptualization: Nicholas McCarthy, Adrien Guyot
Data curation: Alex Terrasson
Formal analysis: Alex Terrasson, Nicholas McCarthy, Andrew Dowdy, Harald Richter, Adrien Guyot
Funding acquisition: Nicholas McCarthy, Andrew Dowdy, Hamish McGowan, Adrien Guyot
Investigation: Alex Terrasson, Nicholas McCarthy, Andrew Dowdy, Harald Richter, Adrien Guyot
Methodology: Alex Terrasson, Nicholas McCarthy, Adrien Guyot
Project administration: Hamish McGowan, Adrien Guyot
Supervision: Nicholas McCarthy, Hamish McGowan, Adrien Guyot
(continued)

1. Introduction

The complex interactions between weather, fuels, and anthropogenic influences (including relating to fire ignition and fire suppression activities) make accurate predictions of extreme wildfire difficult. The influence of climate change on wildfire risk factors presents additional challenges in relation to long-term planning for wildfire management (Abatzoglou & Williams, 2016; Dowdy & Pepler, 2018; Flannigan et al., 2009). Concurrently, changes in rural activities including the urban sprawl into wildland regions (Radeloff et al., 2005), as well as the "tree change" phenomenon where residents seek to escape city life by moving into rural areas, are resulting in an increasing population in many wildfire prone regions. One of the acute manifestations of this combination of factors is the occurrence of extreme wildfires that cause severe damage.

Extreme wildfires with large convective plumes capped by deep cumulus clouds (pyroCu) may form pyrocumulonimbus (pyroCb; American Meteorological Society, 2016; Peterson et al., 2017), also described as "fire-triggered thunderstorms" (Carrier et al., 1985; Finney & McAllister, 2011; Mitchell et al., 2006; Rosenfeld et al., 2007). PyroCb have the potential to dramatically affect fire spread due to intense spotting, new lightning ignitions (Dowdy et al., 2017), and modification of the near-surface wind field (Peace et al., 2017), all of which can lead to unpredictable and dangerous changes in fire activity. Such

Visualization: Alex Terrasson, Adrien Guyot
Writing - original draft: Alex Terrasson, Andrew Dowdy, Adrien Guyot
Writing – review & editing: Alex Terrasson, Nicholas McCarthy, Andrew Dowdy, Hamish McGowan, Adrien Guyot

storms also have important implications for atmospheric chemistry as they may inject aerosols and trace gases into the stratosphere (Fromm et al., 2006; Luderer et al., 2006). The large extreme wildfires associated with pyroCb are often the most destructive, resulting in substantial economic costs and loss of life (Tedim et al., 2018). Recent research suggests that climate change may increase the likelihood of dangerous risk factors associated with pyroconvection in the western United States, specifically in the mountainous regions (Luo et al., 2013) as well as southern and eastern Australia (Dowdy & Pepler, 2018). Additionally, pyroCb activity can also influence the climate, with stratospheric injection of smoke able to significantly perturb the lower stratosphere through processes similar to volcanic intrusions (Peterson et al., 2018).

Research of pyroCb has primarily been centered on cases in western North America and temperate regions of Australia, regions that appear to have favorable environmental conditions for their formation (Dowdy & Pepler, 2018; McRae et al., 2015; Peterson et al., 2017). The conditions associated with pyroCb genesis include dry fuels and an ignition source, a dry boundary layer often with moister conditions in the midtroposphere and a steep temperature lapse rate, a middle-upper level disturbance (which can potentially help trigger the convection in some cases), and extensive heat and moisture release from combustion (Dowdy et al., 2017; Peterson & Wang, 2013; Peterson et al., 2017), although the exact contribution of each of these factors is not certain. Peterson et al. (2017) proposed a conceptual model for pyroCb formation in western North America, concluding that atmospheric conditions must be favorable for high-based convection. A midtropospheric layer of sufficient moisture (Dowdy et al., 2017; Peterson et al., 2017) is also beneficial as this can enhance vertical column development through reduced entrainment of dry air, condensation, and latent heat release enabling strong updrafts for the fire plume to reach the upper troposphere. Fromm et al. (2006) describe a "violent pyroconvective storm" that impacted heavily on Canberra (Australia) in 2003, which generated hail and a nonsupercell tornado (McRae et al., 2013).

As a convective plume intensifies and begins to initiate moist convection, the origins and effects of associated turbulence remain largely unknown. This is despite the fact that turbulence has recently been shown to be one of the most critical drivers of extreme fire behavior (McRae et al., 2013; Thurston et al., 2017). Vortices will often develop within the smoke plume and the pyroCb at multiple scales in time and space (Forthofer & Goodrick, 2011). These coherent turbulent eddies are capable of bridging the scales from micrometeorological combustion dynamics up to storm-scale meteorology, though few observations of such vortices exist (McCarthy et al., 2018; McRae & Flannigan, 1990). Addressing the gaps in knowledge on such physical processes, which do interact between these scales, is critical to better prediction of extreme fire behavior, but there is a dearth of quantitative observations on such processes, especially in the context of the pyroCb life cycle.

Operational and mobile weather radars have been used widely to observe and help understand mechanisms leading to thunderstorm genesis and development (Bringi & Chandrasekar, 2001), including the quantification of turbulence and large-scale vorticity (e.g., radius 1–10 km; Lareau & Clements, 2016; Rosenfeld et al., 2007; Williams et al., 2006). There is increased interest in the use of weather radar to monitor plumes and the behavior of wildfires (Duff et al., 2018; McCarthy et al., 2018). However, no studies to date have used weather radar data to detail a fire-trigged thunderstorm life cycle in conjunction with quantitative fire spread observations.

The Sir Ivan Dougherty fire in eastern Australia provided an opportunity to examine previously unexplored aspects of extreme pyroconvection. The fire impacted 55,000 ha of land in New South Wales, between 11 and 17 February 2017, with the most extreme fire behavior occurring on 12 February including rapid increases in fire spread, the occurrence of a pyroCb (Figures 1 and 2), and severe impacts on the region's rural community (including extensive losses of livestock, houses, and infrastructure).

Here we present observations of the life cycle of the Sir Ivan Dougherty fire pyroCb with associated mesoscale atmospheric and land surface conditions using operational S-band Doppler radar, atmospheric soundings, and surface micrometeorological observations. Analysis of time series of volumetric radar variables characterizing grid-scale turbulence and the formation and evolution of kilometer-scale vortices are presented. The aim is to better understand the processes leading to pyroCb genesis, growth, and decay to improve prediction of wildfire-atmosphere interaction and mitigate risk to life and property from extreme wildfires.

Figure 1. Photograph showing the pyroCb on 12 February 2017 at 5:30 UTC, taken at location 31.915857ºS, 149.667840ºE near the local town of Coolah, looking to the southeast (Credit: Alex Ellinghausen).

2. Data and Methods

2.1. Observations of the Sir Ivan Dougherty Fire

The Namoi Doppler radar is part of the Australian radar network operated by the Bureau of Meteorology (BoM). It is located on the Blackjack Mountain, 115 km north northeast from the ignition location of Sir Ivan Dougherty fire, at an elevation 270 m above the point of ignition (Figure 3). This radar operates using a 10-cm wavelength (S-Band), has low attenuation, and is sensitive to large (millimeter-scale) ash and debris but not to cloud droplets and micron-scale smoke (Lareau & Clements, 2016; McCarthy et al., 2018). Over the fire ground (115 km from the radar), gate spacing is approximately 500 m. A 14-elevation scan pattern (between 0.5° and 32°) forms a volume every 10 min in the set operational scan pattern.

Radar data were preprocessed on site: First, ground clutter was reduced using a fast Fourier transform analysis-based method. Radar volumes with excessive clutter reduction (Z > 25–30 dBZ) were removed.

Figure 2. Photograph showing the pyroCb on 12 February 2017 at 6:15 UTC, taken at location 31.915857ºS, 149.667840ºE near the local town of Coolah, looking to the southeast (Credit: Alex Ellinghausen).

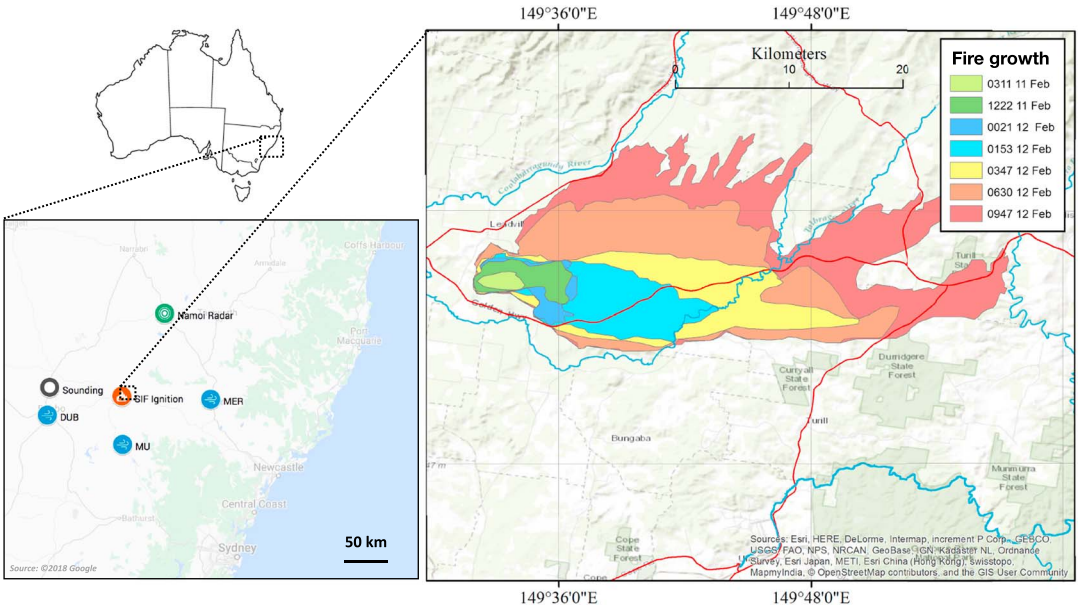

Figure 3. (left panels) The location of Sir Ivan Dougherty fire in Northern New South Wales (Australia), the location of the Namoi radar (green), the fire ignition point (red), together with the surrounding Bureau of Meteorology weather stations (blue) and the Rural Fire Service sounding location (black). (right panel) The isochrones of fire spread between 0311 UTC on 11 February 2017 and 0947 UTC on 12 February 2017, as observed by the Rural Fire Service.

Threshold quality control was subsequently applied on the reflectivity and the signal quality index to remove noise from the observations. The active fire area of the Sir Ivan Dougherty incident was within the Namoi radar's range for the entire event, and the radar was used to measure equivalent reflectivity, radial velocity, and spectrum width. The lowest measured plume signatures were observed at around 2,000 m above sea level. We also derive an echo top field, defined as the highest level at which the radar reflectivity exceeds 18 dBZ (Lakshmanan et al., 2013), as a relative indicator of convective intensity through time and space.

Surface atmospheric observations were sourced from automatic weather stations operated by the BoM at locations surrounding the fire (Figure 3). In particular, barometric pressure, air temperature, relative humidity, and wind speed and direction were used to estimate the timing of the passage of a cold front and the preceding trough (Figure 4). The New South Wales Rural Fire Service operates a mobile atmospheric sounding system and was able to conduct observations of atmospheric profiles of air temperature, humidity, and wind (Figure 5). Satellite observations (Himawari-8) were used to identify the onset of pyroconvection using the visible (shortwave) bandwidth, are shown concurrently with radar data, and are provided in subsequent discussion.

On the morning of the pyroCb event (at 2200 UTC on 11 February 2017, 0900 AEDT) the fire weather conditions were already extreme, including 18% relative humidity, wind speeds of 17 m/s, and surface temperatures of 36 °C which later reached a maximum of 43.5 °C. A measure of fire weather commonly used in Australia (Dowdy, 2018), the Forest Fire Danger Index (McArthur, 1967) had values of around 90, which exceeded the 10-year return period based on a data set of daily values back to 1950 (Figure 6). Fires burning in these conditions are extremely difficult to control, noting that the fire breached containment lines on this day.

During the afternoon on that day (at around 0520 UTC on Sunday, 12 February 2017, 1620 AEDT), a cold front passed over the fire, spreading the fire toward the northeast. The change in wind direction from the northwest to the southwest helped facilitate the change in fire spread direction, with the northern flank of the fire then becoming the new fire front. This increase in the effective length of a fire front, as the region that was previously the flank prior to a wind direction change, is a well-known process for increasing the rate of fire spread. A pyroCb formed between 0530 UTC and 0700 UTC (Figures 1 and 2) and produced lightning (Figure 4 and supporting information Figure S1) before fire activity subsided at night. Infrared imagery observations (Himawari-8) and lightning data suggest that pyroCb activity (attached to the fire) was

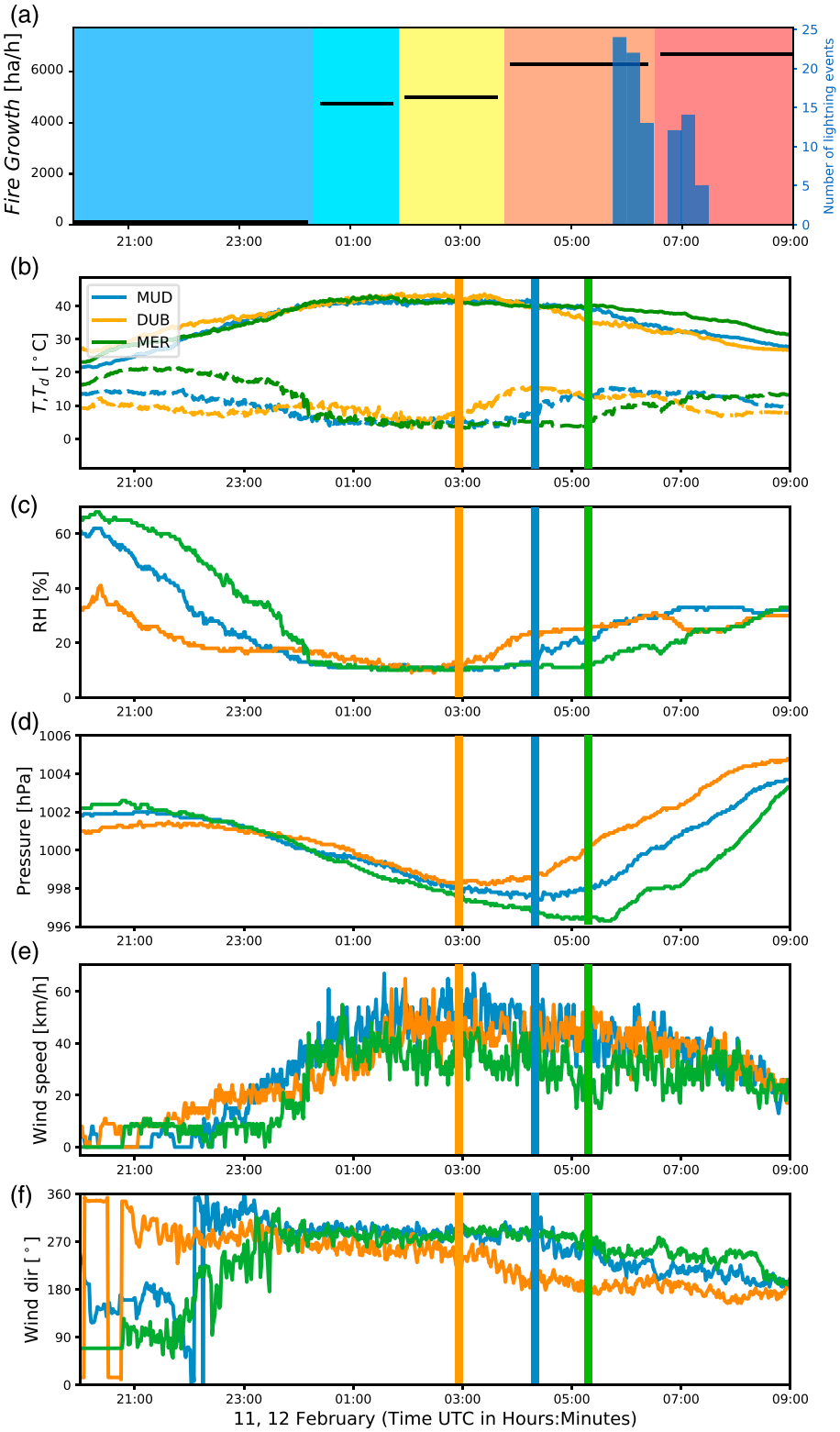

Figure 4. Time series during 11–12 February 2017 (in UTC) of (a) fire growth (ha/hr; as observed by Rural Fire Service) as well as lightning events (number of events every 15 min, from the commercial provider Global Position And Tracking Systems (GPATS) Australia), (b) air temperature and dew point temperature (°C), (c) relative humidity (%), (d) surface pressure (hPa), (e) wind speed (km/hr), and (f) wind direction (degrees) observed at automatic weather stations at Mudgee (blue), Dubbo (orange) and Merriwa (green) operated by the Bureau of Meteorology. Locations of stations are shown in Figure 3. MUD = Mudgee; DUB = Dubbo; MER = Merriwa.

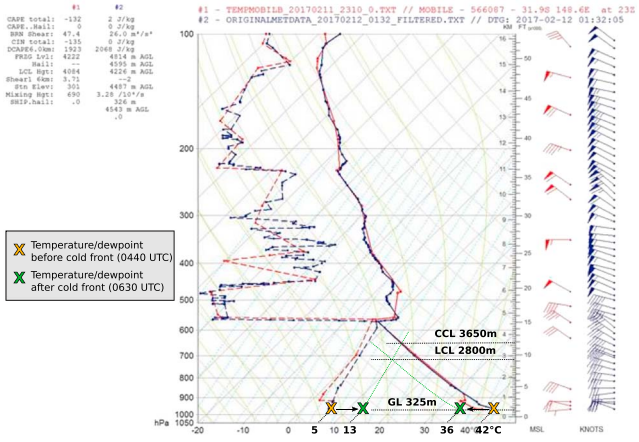

Figure 5. Atmospheric Soundings taken at 2310 UTC on 11 February 2017 (red) and 0132 UTC on 12 February 2017 (blue) at 31.9°S and 148.6°E. Black and blue crosses show surface dew point and temperature, respectively, before and after the cold front passage. Lifted Condensation Level (LCL) and Convective Condensation Level (CCL) after cold front are graphically derived respectively at 2,800 and 3,650 m above sea level (or 2,475 and 3,325 m above Ground Level (GL)).

present for approximately 60 min. This represents a set of conditions typical of many of the most devastating fire events that have occurred previously in southern and eastern Australia. The New South Wales Rural Fire Service compiled a chronology of that event, including firefighters' testimonies that the lightning generated in the fire plume ignited new fires well ahead of the fire front (https://spark.adobe.com/page/qKrHHzFo3pjKF/).

2.2. Measure of Turbulence Intensity per Radar Volume

Energy dissipation rate (EDR) was computed from radar data. It represents the amount of energy lost by viscous forces in the turbulent flow (Doviak & Zrnic, 1993). Turbulent intensity has long been known to be connected to radar spectrum width, which is defined as the standard deviation of velocity distribution within a single pixel. However, spectrum width is sensitive to low signal-to-noise ratio (Bohne, 1982). Therefore, an algorithm including data quality control was necessary. We used the NTDA algorithm (NCAR Turbulence Detection Algorithm), initially developed for real-time measurements of turbulence for aircraft safety purposes (Labitt, 1981). Williams et. al., (2006) compared in situ EDR data and NTDA output to test the algorithm performance and found good correlation, with substantial spread in NTDA EDR estimates and a positive bias of about 0.15 $m^{2/3}/s$ (Williams & Meymaris, 2016).

The wildfire plume EDR was computed from the Namoi radar reflectivity, Doppler velocity, and spectral width and transposed to a three-dimensional Cartesian mesh grid using Kriging (Williams et al., 2006). Data quality control was performed in two steps: (i) data censoring to remove artifacts among radial velocity and spectrum width, and (ii) a confidence coefficient C_{SW} was computed and assigned to each spectrum width signature. This confidence coefficient (used in equation (2)) is a geometric average of confidence intervals for different radar returns (Williams et al., 2006). In practice, a raw EDR is initially calculated for each radar gate using equation (1):

$$EDR_{\mathrm{raw}}(r) = SW(r).f(r, L_0) \tag{1}$$

where $SW(r)$ is the quality-controlled spectrum width, $f(r, L_0)$ is a scaling function obtained via a theoretical function based on radar assumptions (Cornman & Goodrich, 1996), r is the radial distance (meters) from the radar, and L_0 is the turbulence outer length scale. The final EDR is computed on a mesh grid generated by the algorithm and is a local mean weighted by the confidence coefficient (equation (2)):

$$EDR(r) = \sqrt{\frac{\sum_{r(i)\in D} C_{SW}(r(i)) EDR_{raw}(r(i))^2}{\sum_{r(i)\in D} C_{SW}(r(i))}} \tag{2}$$

where D is a disk around the point r, and $C_{SW}(r(i))$ is the confidence associated with $SW(r(i))$. This algorithm has been shown to provide good quality control and reliable turbulent intensity measures (Lang & Guy, 2017).

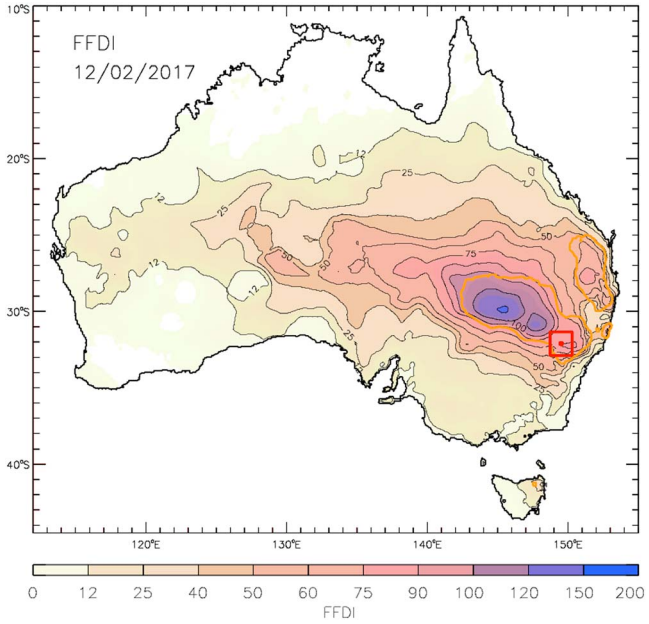

Figure 6. McArthur Fire Danger Index (FFDI) for 12 February 2017, based on a gridded analysis of observations (Dowdy, 2018), with the location of the Sir Ivan Dougherty fire shown (red dot). The orange contour line shows the region with FFDI above its 10-year return period, calculated for each individual location using daily data from 1950 to 2016.

3. Results

3.1. Meteorological Background and Fire Behavior

The fire growth is shown in Figures 3 and 4. The maximum fire growth was reached in the early evening: 6700 ha/hr burnt between 0630 and 0940 UTC. The maximum in fire growth followed the passage of the cold front (passing through the fire from 0520 UTC) and the pyroCb (lasting from about 0500 to 0700 UTC, as detailed in section 3.2).

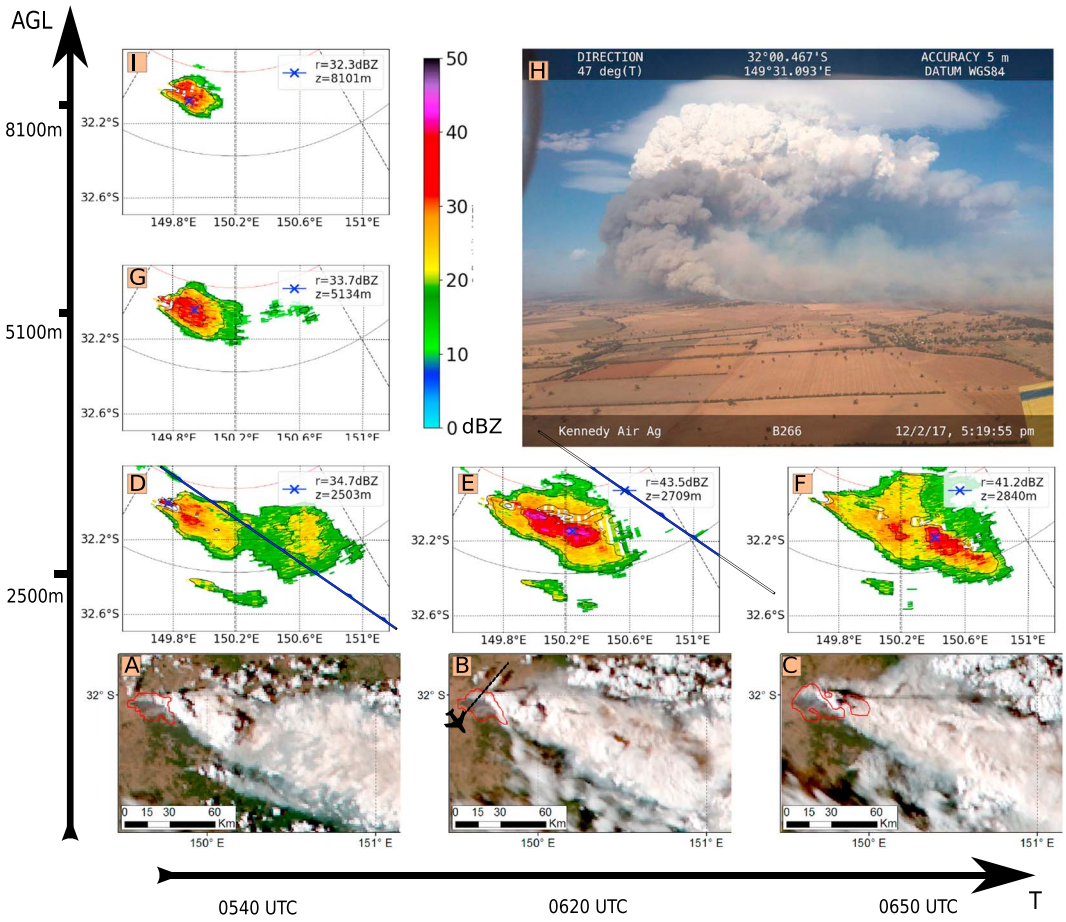

Figure 7. (a–c) The Himawari 8 VIS picture of the plume at 0540, 0620, and 0650 UTC. Red shapes are the burning areas. (d–f) The Namoi radar reflectivity signatures of the plume for 0.5° beam elevation (beam altitude over the fire between 2,500 and 3,200 m above ground level) at 0540, 0620, and 0650 UTC. (g, i) The plume at 0540 UTC for two additional elevations (5,100 and 8,100 m). (h) Image of the pyroCb taken by the New South Wales Rural Fire Service at 0620 UTC (photographer's aircraft location is displayed in panel b). Blue cross and blue line respectively show the maximum of reflectivity and the cold frontal passage when detectable.

Prior to the passage of the front, the conditions were not conducive to the development of deep convection, as indicated by the soundings in Figure 5. A well-mixed deep boundary layer was capped by a strong inversion near 550 hPa leading to zero surface-based convective available potential energy (SBCAPE). After the cold front passed over the fire ground around 0600 UTC, the environmental conditions temporarily became more favorable for deep convection due to an increased surface dew point combined with only slowly decreasing surface temperatures (see Figure 4). The initial 42/5 °C surface parcel (notation: surface air temperature/surface dew point) transitioned into a 36/13 °C parcel after the cold front passage (see Figure 5), greatly enhancing its SBCAPE value. Within the first hour after the passage of the surface front, surface parcels reached a temporal maximum in SBCAPE just behind (or south of) the cold front. The increase in surface moisture content outweighed the decrease in surface temperature in terms of their respective contributions to the surface parcel energy. Consequently, the relatively rapid increase in moisture combined with the slower decrease in temperature created a postfrontal corridor of SBCAPE that helped provide conditions favorable for deep convection to occur. Further on, the surface temperature decreased by an average rate of 3.2 °C/hr, which could plausibly act to dampen the fire growth.

The postfrontal boundary moisture increase alone was not sufficient to produce thunderstorms, except in the proximity of the fire itself. We define "the plume" as the whole smoke volume including the pyroCb. Lightning observations (Figure 7) clearly show a strong cluster of activity around the plume downwind of the fire during the hour of 0500 UTC (1600 AEDT) when the frontal system passed over the fire ground, with no other lightning strikes observed in the surrounding region including elsewhere along the cold front.

Observations of lightning associated with the plume provide direct evidence of deep convection including strong updrafts required for charge separation needed for generating lightning (Dowdy et al., 2017; Lang & Rutledge, 2002). This indicates that while the frontal passage helped provide broad-scale conditions conducive to deep convection, the fire modification of the localized near-surface conditions was necessary to trigger the thunderstorm activity, given that lightning did not occur at other locations along the front further away from the fire plume. The role of the fire-atmosphere interactions in generating the observed thunderstorm characteristics therefore provides evidence of this event as being a pyroCb, as distinct from a nonpyrogenic thunderstorm or a pyroCu (pyrocumulus: i.e., a moist convective fire plume but without lightning generation).

3.2. Plume Structure and Development

Plume development and characteristics as captured by visible satellite imagery (Himawari 8) and the Namoi radar reflectivity are shown in Figure 7. Due to the distance to the radar, only radar scans above 2,500 m AGL (above ground level) are provided. We identify three dominant modes of the plume on 12 February: before 0520 UTC (prior to the pyroCb formation and the cold frontal passage), between 0520 and 0600 UTC (during pyroCb initiation and growth over the plume coinciding with the passage of the cold front), and after 0600 UTC (when the pyroCb decouples from the fire, matures and subsides). Before 0520 UTC, the plume expanded toward east southeast over a distance of 110 km. Observed echo tops and maximum of reflectivity remained respectively under 7,500 m AGL and 35 dBZ.

Between 0520 UTC and 0600 UTC, the initially shallow cold frontal wind and air mass change affected the burning area and the lower part of the plume, splicing the plume along a horizontal plane from the resulting wind shear. The lower segments of the plume started to move to the northeast, while the upper segments continued east southeast aligned with the upper-level flow (Figure 7). This is shown in Figure 7d: As the cold front (indicated by the blue line) passed through the plume, two distinct reflectivity cores (>20 dBZ) appeared. The pyroCb underwent rapid development between 0520 and 0530 UTC. The top cloud brightness temperature observed by Himawari-8 (10.4-μm window) at this time went below the broadly accepted −40 °C threshold for significant pyroCb clouds (Rosenfeld et al., 2007). Additionally, the derived echo tops increased from 6,500 to 12,700 m between 0510 and 0530 UTC; leading to an average ascent rate of 5.12 m/s at the 18-dBZ plume top. Of note, the pyroCb grew as a nearly vertical column during this 20-min period. This feature was located at 149.85°E, 32.02°S, directly above the active fire and presented a maximum reflectivity exceeding 30 dBZ.

The pyroCb's reflectivity core can be seen in Figures 7d, 7g, and 7i, showing quasi-horizontal plume cross sections at 2,500, 5,100, and 8,100 m AGL, respectively, at 0540 UTC. By 0550 UTC, the BoM had advised that a pyrocumulonimbus had formed above the Sir Ivan fire, and firefighters were instructed to work on the fire from safe distances only and to expect lightning on the fire ground (Whittaker & Taylor, 2018). The observed plume growth from the Sir Ivan Dougherty fire was nonuniform: During the pyroCb growth (0520 to 0540 UTC volumes) the area of reflectivity greater than 30 dBZ was 5 times larger in the 5,000-m scan than in the 2,500-m AGL scan. This can be explained by the larger hydrometeors at 5,000 m (large droplets and ice with water layer) forming larger radar targets, manifesting in the stronger reflectivity signatures. In maturing, the plume saw rapid increase in volume and intensity associated with the pyroCb growth. The total volume above 2,500 m (computed from the radar scan as volume where $Z > 2$ dBZ) increased by 20% (from 1.22 10^4 km^3 at 0510 UTC to 1.48 10^4 km^3 at 5:40 UTC), while the volume for $Z > 30$ dBZ grew by a factor of 22 (from 4.37 10^1 km^3 at 0510 UTC to 9.83 10^2 km^3 at 0540 UTC). These features are also displayed in Figure 8, where reflectivities and $EDR^{1/3}$ distributions in volume within the plume are plotted from 2 hr prior the cold front passage (0320 UTC) to 3 hr after (0820 UTC).

From 0600 UTC onward, the pyroCb started to show signs of thunderstorm decay. Echo tops decreased from 12,200 m at 0600 UTC to 8,300 m at 0700 UTC. At 0600 UTC, the cross-sectional area for $Z > 30$ dBZ was 480 km^2 at 5,100 m and 317 km^2 at 2,500 m. At 0620 UTC, these areas were similar, indicating a weakening updraft and hydrometeors dilution. A large high-reflectivity cell (Figure 7d, cross section of 490 km^2 at 2,500 m) was observed from 0600 UTC between 2,500 and 4,000 m. The cell steered toward east southeast (Figures 7e and 7f).

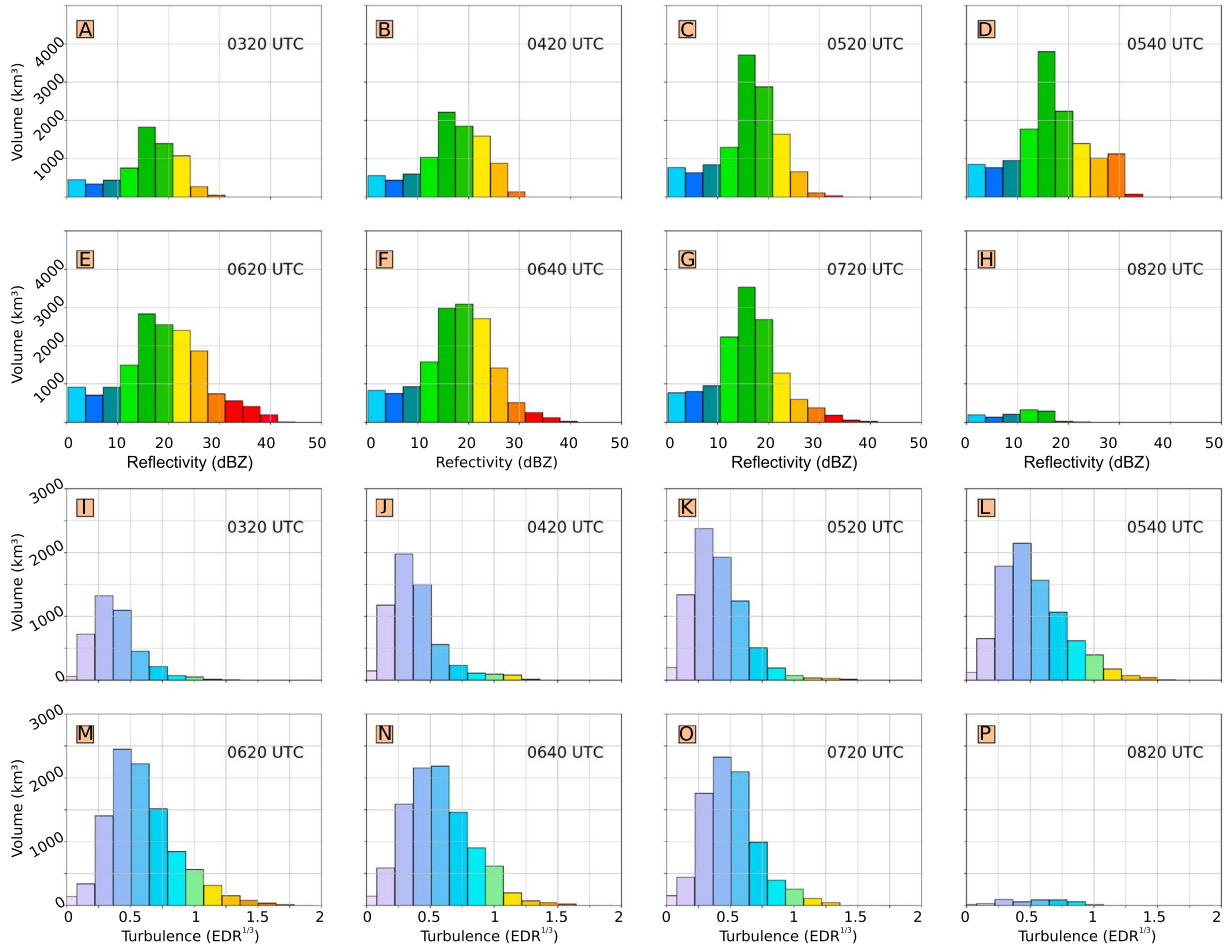

Figure 8. (a–h) The volume distribution for reflectivity Z (dBZ) between 0320 and 0820 UTC. (i–p) The volume distribution for $EDR^{1/3}$ for the same time window. EDR = energy dissipation rate.

3.3. Turbulence and Vortices Within the Plume

Turbulence and circulation analysis were applied to radar data from the genesis, growth, and decay of the pyroCb and plotted in Figure 9. Before 0520 UTC (prior to pyroCb formation), the turbulence shows a maximum at the edge of the plume (see Figure 9a), while Doppler velocity in Figure 9b shows no signs of plume-scale circulations. At 0530 to 0540 UTC, during the pyroCb formation, increased turbulence was present at the center of the updraft (see Figure 9c showing EDR at 0540 UTC and at 8,100 m AGL). Between 0500 and 0540 UTC (prior to and after the pyroCb growth), the total volume of plume ($Z > 2$ dBZ) increased by 26% (from $1.17 \cdot 10^4$ to $1.48 \cdot 10^4$ km^3). During the same period, the volume of turbulence above 1.0 EDR grew by a factor 3.2 (from $1.66 \cdot 10^2$ km^3 at 0500 UTC to $7.06 \cdot 10^2$ km^3 at 0540 UTC). Additionally, the observed maximum in EDR increased from 1.2 to 1.65 $m^{2/3}/s$. Consequently, while the plume increased slowly in volume, simultaneously the measure of turbulence per volume unit increased rapidly.

Turbulent structures and vortices below 4,000 m appeared from 0620 UTC, after the pyroCb growth phase and passage of the cold front when maximum EDR increased from 1.65 to 2 $m^{2/3}/s$ between 0540 and 0620 UTC. Spatial distribution of turbulence migrated from the edge of the pyroCb to its core, organized as a line oriented northwest to southeast, parallel to the orientation of the surface front which suggests the frontal boundary might have created an environment conducive to storm-scale rotation and turbulence (see Figures 9d, 9f, 9h) and located at the edge of the high cell of reflectivity mentioned in section 3.2. Two larger circulation signatures appeared after 0620 UTC. They formed and moved along the centerline of the plume below 4,000 m (Figures 9e, 9g, and 9i). The radial shear associated with these vortices was 15 to 20 m/s over an azimuthal distance of up to 10 km. Available data could not show if these vortices originated from

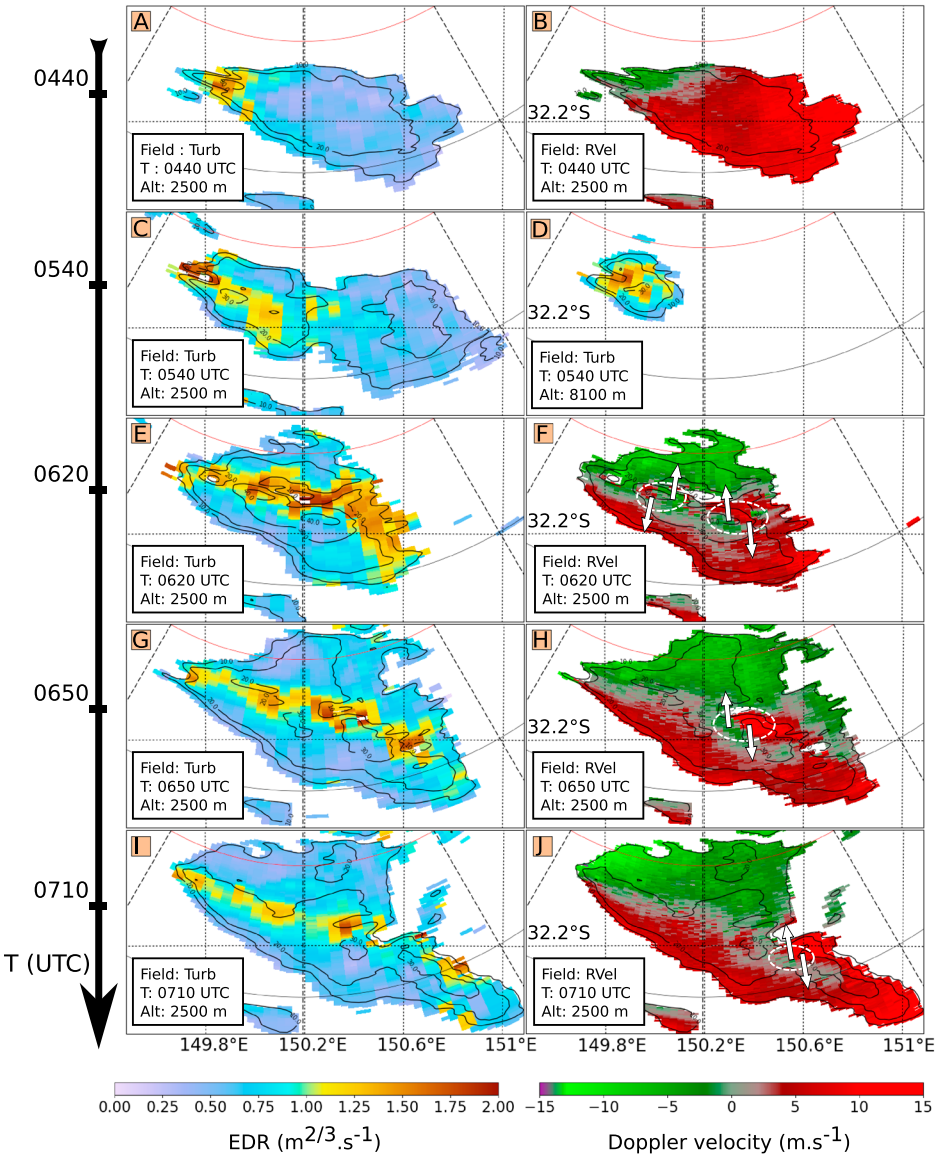

Figure 9. Timeline of the turbulence and radial velocity between 0440 and 0710 UTC on 12 February 2017. In each panel, Turb stands for turbulence (a filter was applied to improve visualization; see supporting information Figure S3 for details). RVel = radial/Doppler velocity; Alt = the average altitude of the radar signatures. An Alt value of 2,500 m corresponds to a signature between 2,200 and 3,200 m above ground level, and 8,100 m to signatures between 7,800 and 8,300 m above ground level. Larger-scale vortices (panels f, h, and j) are highlighted. Solid black contours denote smoothed reflectivity values of 10, 20, 30 and 40 dBZ.

the surface upward as per a fire whirl or within the pyroCb in a rotating updraft. One plausible physical mechanism proposed here for their formation mechanism relates to the vertical wind shear that accompanies a frontal system such as the one that passed over the fire ground at that time, with the tilting of horizontal ambient wind shear via convective updrafts being a known formation mechanism for supercell thunderstorm development (Rotunno & Klemp, 1982). Overall, radar data showed discrete features along the pyroCb centerline both at large scale (vortices) and small scale (high turbulence) after the cold front passage and during the decaying phase of the pyroCb. We hypothesize that the passage of the surface cold front and subsequently deepening colder air mass with flow from the southwest supplied enhanced horizontal vorticity to the strengthening updrafts. The strengthening updrafts during the pyroCb growth phase were likely associated with tilting this vorticity into the vertical axis, which is illustrated by circulations as shown in Figure 9. This mechanism of tilting horizontal vorticity is similar to

the formation of storm-scale circulation in intense thunderstorms (without a fire) known as supercells (Rotunno, Klemp et al. 1982). While still representing a hazard to firefighting operations, the decay phase of the pyroCb was most likely a decoupled process from the fire behavior where the heat and moisture of the fire were no longer feeding updrafts.

4. Discussion

The Sir Ivan Dougherty fire is a case where a severe thunderstorm formed in a region collocated with the fire plume, in contrast to some previous studies of thunderstorm activity over wildfires where the primary physical mechanism being observed was the ingestion of wildfire smoke by thunderstorms which happen to be passing over the fire ground (Rudlosky & Fuelberg, 2011). In particular, we consider the term pyroCb to refer to cases where the influence of the fire is an essential ingredient for a given set of environmental conditions, without which a thunderstorm would not occur. This is clearly demonstrated to be the case for the Sir Ivan Dougherty fire based on the results presented here, including due to the observed lightning activity only occurring around the fire plume but not around the surrounding region more broadly (supporting information Figure S1). The subsequent fire ignition caused by this pyrogenic lightning is also noteworthy, as this has only been presented once in the literature previously (Dowdy et al., 2017), with the limited focus of studies on the fire-atmosphere coupled feedback process (i.e., new fires ignited by pyrogenic lightning) providing considerable scope for future research efforts.

Previous studies of extreme pyroconvection (including pyroCu and pyroCb) have primarily focused on thermodynamic rather than dynamic factors that can influence thunderstorm formation in a fire plume. Thermodynamic factors include the heat and moisture release from the fire which can significantly modify the thermodynamic properties of an air parcel, in addition to the surrounding environmental conditions such as low-level moisture and temperature lapse rates (as can be indicated by measures such as CAPE; Peterson et al., 2017; Tory et al., 2018). In relation to pyroCu and pyroCb formation, these thermodynamic conditions have the potential to lead to strong updrafts that characterize severe thunderstorm activity. Although dynamical influences on pyroCb formation have not been a key focus of most studies, the importance of their role was demonstrated by a rare case of a pyroCb that initiated around midnight on Black Saturday in February 2009 in southeast Australia (for the Beechworth fire as detailed in Dowdy et al., 2017). For that event, the fire's influence on the atmospheric conditions was not enough to produce a pyroCb during the day, with the pyroCb initiated only around midnight with the passage of an undular bore over the fire ground. A modeling study showed a region of uplift associated with the bore as well as with an earlier cold front concurrent with the formation of the bore (Engel et al., 2013), with the uplift representing an additional dynamical factor to trigger thunderstorm activity. For the Sir Ivan Dougherty fire, the passage of the cold front around the time of storm intensification (e.g., as indicated by the lightning activity) highlights a potential dynamic influence on the formation of the pyroCb. In particular, uplift associated with the front, as well as horizontal shear, provided a potential source of vorticity for influencing thunderstorm organization in addition to the fire's influence on the thermodynamical properties of the near-surface air parcels that form the base of the fire plume. Collectively, these factors lead to the formation of a severe fire-initiated supercell thunderstorm, which displayed large-scale rotation. Observed velocity couplets in this study are within the range of 15 to 20 m/s (Figure 9). This is within and in the lower range of values observed with Doppler weather radars for mesoscale circulation in North American supercell thunderstorms (Kumjian & Ryzhkov, 2008), while tornadic events will typically see velocity couplets of above 25 m/s (Bluestein et al., 2007). It is also noted that a wind change associated with a front can influence fire behavior (e.g., the flank of a fire can become a long fire front resulting in changes to a fire's characteristics including its size and intensity), therefore impacting the fire's influence on the atmosphere. Given the range of factors that can influence pyroCb formation, examples such as the Beechworth pyroCb as well as the Sir Ivan Dougherty fire presented here suggest that a research priority for future studies should be on the influence of fronts on fire behavior and atmospheric thermodynamics on pyroCb. In particular, attention is needed in cases where fire-coupled thunderstorms become severe, leading to development of supercell thunderstorms with mesocyclone features normally associated with extreme meteorology including large hail, tornadoes and severe winds caused by downbursts. These meteorological hazards may adversely impact the fire ground and greatly increase risk to persons engaged in fire management and suppression activities (Potter & Hernandez, 2017).

PyroCb genesis and evolution have been studied with weather radar often in conjunction with additional satellite remote sensing and fire behavior observations. In most of the cases, studies have been limited to the use of echo tops to produce time series of cloud height, as seen in the signature of radar reflectivity (Rosenfeld et al., 2007). This offered deep pyroconvection studies the possibility to quantitatively link fire behavior to time series of plume development (Dowdy et al., 2017; Fromm et al., 2012; McRae et al., 2015). Furthermore, analysis of these time series enabled quantitative estimates of velocities (mostly vertical) as described in Potter (2012). Conversely, very few studies (Banta et al., 1992; McCarthy et al., 2018) have used radar Doppler data to study the dynamics of pyroCb, including the occurrence of vorticity and shear. Peace et al. (2017) described the genesis and growth of two pyroCbs in Western Australia, forming on a slope gradient with a sea breeze boundary, therefore presenting similarities with the case presented here. The sea breeze, a weaker near-surface boundary as compared to the cold front presented here, was promoting the existence of an updraft as seen in their radar data from the lowest elevation scan. These boundaries (e.g., cold front, sea breezes, and outflow boundaries) can provide enhanced horizontal and vertical vorticity to an updraft, which, via the tilting and stretching mechanisms, can enhance the likelihood of midlevel rotation in the updraft. Boundaries similar to a cold front can possibly be other preferred regions where collocated updrafts are more likely to develop rotation as seen with the Sir Ivan Dougherty fire, as compared to updrafts not connected to any noteworthy boundary. Further pyroCb studies should try to incorporate observations of radar Doppler velocities and EDR when possible, to further document these boundary mechanisms favoring updrafts, vorticity, and convective initiation.

5. Conclusion

Here, we presented the case study of a wildfire that occurred in an atmospheric setup commonly associated with extreme fire events in southeast Australia during the summer. The fire developed during extreme fire weather conditions and was subsequently influenced by an abrupt change in meteorology, that is, the passage of a cold front with a wind direction change causing an increased rate of fire growth.

The fire was very active before the passage of the cold front, but above the fire, the plume was relatively weak with limited column development. The passage of the cold front brought a northwest-to-southeast oriented corridor of instability at the lower levels, including by increasing the surface dew point temperature, while the surface temperature decreased only gradually in the postfrontal air mass. The cold front had both a "dampening" (lower temperature, more humidity) and an "enhancing" impact on the fire behavior: It created a new fire front (oriented northwest to southeast) and maintained a sustained fire growth (increased fire front). The latter increased the temperature and moisture content of the air in the fire plume, which can further help increase the potential for convective processes to occur. The frontal passage led to an increase in ambient moisture at low levels (unstable layers with high dew point observed after the front passage). This unstable air just behind the front was subsequently lifted and enhanced pyroCb growth. This mechanism of growth could only occur if the cold front was not too deep; for example, timing, cold frontal depth, and its properties (temperature and moisture content) need to be optimum to trigger pyroCb growth. In addition to thermodynamic mechanisms, our findings suggest that the cold front-enhanced horizontal shear and the associated horizontal vorticity was tilted into vertical vortices from the updrafts above the fire. This highlights the potential role of vertical motion associated with cold fronts as a dynamic mechanism that could help trigger pyroCb formation. The narrow band of strong turbulence (i.e., EDR) and the formation of kilometer-scale vortices at midlevels is potentially the result of the migration of vortices from the plume edges to the interior, considerable lighting activity was observed near the fire ground after the passage of the cold front. This is linked to an increase of moisture and the presence of large amount of cloud condensation nuclei, which could influence the electrification of the pyroCb.

In-depth analysis of high-resolution volumetric radar data is shown to be critical in improving our understanding of the fire behavior, plume, and storm development and the interaction with the surrounding atmospheric setup. The capacity for operational weather radar to derive fine temporal resolution quantitative estimates of wind velocity within the plume, plume contours, intensity, and scale of turbulence and vortices has been demonstrated. We highlight the usefulness of deriving secondary weather radar moments such as EDR, which can help understand mechanisms triggering pyroCb formation and growth. Additionally, it has the ability to quantify these factors between plumes of different fires, enabling better decision making in

resource tradeoffs. Given its unique quantitative capabilities, operational weather radar data should be used more systematically. In conjunction with fire behavior information, this will improve nowcasting extreme fire behavior and associated fire-trigged thunderstorms, as well as in-depth postevent analyses to better understand processes and mechanisms linking wildfires and the atmosphere.

Acknowledgments
We thank the New South Wales Rural Fire service for providing radiosonde data and aerial photographs of the fire. A. G. was funded by a Fellowship from The University of Queensland. A. T. was supported by a University of Queensland Collaboration Industry Engagement Fund. N. M. is supported by a PhD top up scholarship from the Advanced Queensland program from the Queensland Government. A. D. was supported by the National Environmental Science Program (NESP). The authors would like to thank Tony Hirst, Kevin Tory, and Alain Protat from the Australian Bureau of Meteorology for their review of the manuscript and constructive comments. We thank the developers of PyTDA for making their code accessible (https://github.com/nasa/PyTDA). Many thanks to Alex Ellinghausen for providing his professional photographs of the fire. Thanks to the three anonymous reviewers and the Associate Editor who provided very constructive comments. The authors declare no conflict of interest.

References

Abatzoglou, J. T., & Williams, A. P. (2016). Impact of anthropogenic climate change on wildfire across western US forests. *Proceedings of the National Academy of Sciences*, *113*(42), 11,770–11,775. https://doi.org/10.1073/pnas.1607171113

American Meteorological Society, 2016: "Pyrocumulonimbus." Glossary of Meteorology. Available online at http://glossaryametsoc.org/wiki/Pyrocumulonimbus

Banta, R. M., Olivier, L. D., Holloway, E. T., Kropfli, R. A., Bartram, B. W., Cupp, R. E., & Post, M. J. (1992). Smoke-column observations from two forest fires using Doppler lidar and Doppler radar. *Journal of Applied Meteorology*, *31*(11), 1328–1349. https://doi.org/10.1175/1520-0450(1992)031<1328:SCOFTF>2.0.CO;2

Bluestein, H. B., French, M. M., Tanamachi, R. L., Frasier, S., Hardwick, K., Junyent, F., & Pazmany, A. L. (2007). Close-range observations of tornadoes in supercells made with a dual-polarization, X-band, mobile Doppler radar. *Monthly Weather Review*, *135*, 1522–1543. https://doi.org/10.1175/MWR3349.1

Bohne, A. (1982). Radar detection of turbulence in precipitation environments. *Journal of the Atmospheric Sciences, Boston*, *39*(8), 1819–1837. https://doi.org/10.1175/1520-0469(1982)039<1819:RDOTIP>2.0.CO;2

Bringi, V. N., & Chandrasekar, V. (2001). *Polarimetric Doppler weather radar: Principles and applications*. Cambridge university press. https://doi.org/10.1017/CBO9780511541094

Carrier, G. F., Fendell, F. E., & Feldman, P. S. (1985). Firestorms. *Journal of Heat Transfer*, *107*(1), 19–27. https://doi.org/10.1115/1.3247379

Cornman, L. B. & R. Goodrich (1996). The detection of atmospheric turbulence using Doppler radars. Workshop on Wind Shear and Wind Shear Alert Systems, Oklahoma City, OK.

Doviak, R. J., & Zrnic, D. S. (1993). *Doppler radar and weather observations*. San Diego, California, USA: Courier Corporation, Academic Press. ISBN: 0-486-45060-0.

Dowdy, A. J. (2018). Climatological variability of fire weather in Australia. *Journal of Applied Meteorology and Climatology*, *57*, 221–234. https://doi.org/10.1175/JAMC-D-17-0167.1

Dowdy, A. J., Fromm, M. D., & McCarthy, N. (2017). Pyrocumulonimbus lightning and fire ignition on Black Saturday in southeast Australia. *Journal of Geophysical Research: Atmospheres*, *122*, 7342–7354. https://doi.org/10.1002/2017JD026577

Dowdy, A. J., & Pepler, A. (2018). Pyroconvection risk in Australia: Climatological changes in atmospheric stability and surface fire weather conditions. *Geophysical Research Letters*, *45*, 2005–2013. https://doi.org/10.1002/2017GL076654

Duff, T. J., Chong, D. M., & Penman, T. D. (2018). Quantifying wildfire growth rates using smoke plume observations derived from weather radar. *International Journal of Wildland Fire*, *27*, 514. https://doi.org/10.1071/WF17180

Engel, C. B., Lane, T. P., Reeder, M. J., & Rezny, M. (2013). The meteorology of Black Saturday. *Quarterly Journal of the Royal Meteorological Society*, *139*, 585–599. https://doi.org/10.1002/qj.1986

Finney, M. A., & McAllister, S. S. (2011). A review of fire interactions and mass fires. *Journal of Combustion*, *2011*, 1–14. https://doi.org/10.1155/2011/548328

Flannigan, M. D., Krawchuk, M. A., de Groot, W. J., Wotton, B. M., & Gowman, L. M. (2009). Implications of changing climate for global wildland fire. *International Journal of Wildland Fire*, *18*, 483–507. https://doi.org/10.1071/WF08187

Forthofer, J. M., & Goodrick, S. L. (2011). Review of vortices in wildland fire. *Journal of Combustion*, *2011*, 984363. https://doi.org/10.1155/2011/984363

Fromm, M. D., McRae, R. H. D., Sharples, J. J., & Kablick Iii, G. P. 2012. Pyrocumulonimbus pair in Wollemi and Blue Mountains National Parks, 22 November 2006. *Australian Meteorological and Oceanographic Journal*, *62*(3), 117.

Fromm, M., Tupper, A., Rosenfeld, D., Servranckx, R., & McRae, R. (2006). Violent pyro-convective storm devastates Australia's capital and pollutes the stratosphere. *Geophysical Research Letters*, *33*, L05815. https://doi.org/10.1029/2005gl025161

Kumjian, M. R., & Ryzhkov, A. V. (2008). Polarimetric signatures in supercell thunderstorms. *Journal of Applied Meteorology and Climatology*, *47*, 1940–1961. https://doi.org/10.1175/2007JAMC1874.1

Labitt, M. (1981). *Coordinated radar and aircraft observations of turbulence* (No. ATC-108). Massachusetts Institute of Technology Lexington Lincoln Lab. Report No. FAA-RD-81-44.

Lakshmanan, V., Hondl, K., Potvin, C. K., & Preignitz, D. (2013). An improved method for estimating radar echo-top height. *Weather and Forecasting*, *28*, 481–488. https://doi.org/10.1175/WAF-D-12-00084.1

Lang, T. J., & Guy, N. (2017). Diagnosing turbulence for research aircraft safety using open source toolkits. *Results in Physics*, *7*, 2425–2426. https://doi.org/10.1016/j.rinp.2017.07.015

Lang, T. J., & Rutledge, S. A. (2002). Relationships between convective storm kinematics, precipitation, and lightning. *Monthly Weather Review*, *130*(10), 2492–2506. https://doi.org/10.1175/1520-0493(2002)130<2492:RBCSKP>2.0.CO;2

Lareau, N. P., & Clements, C. B. (2016). Environmental controls on pyrocumulus and pyrocumulonimbus initiation and development. *Atmospheric Chemistry and Physics*, *16*, 4005–4022. https://doi.org/10.5194/acp-16-4005-2016

Luderer, G., Trentmann, J., Winterrath, T., Textor, C., Herzog, M., Graf, H. F., & Andreae, M. O. (2006). Modeling of biomass smoke injection into the lower stratosphere by a large forest fire (Part II): sensitivity studies. *Atmospheric Chemistry and Physics*, *6*(12), 5261–5277. https://doi.org/10.5194/acp-6-5261-2006

Luo, L., Tang, Y., Zhong, S., Bian, X., & Heilman, W. E. (2013). Will future climate favor more erratic wildfires in the western United States? *Journal of Applied Meteorology and Climatology*, *52*, 2410–2417. https://doi.org/10.1175/JAMC-D-12-0317.1

McArthur, A. G. (1967). Fire behaviour in ucalypt forests. Australia. In *Forestry and Timber Bureau*, (p. 36). Canberra, Australia: Leaflet 107, Forestry and Timber Bureau.

McCarthy, N., McGowan, H., Guyot, A., & Dowdy, A. (2018). Mobile X-Pol radar: A new tool for investigating pyroconvection and associated wildfire meteorology. *Bulletin of the American Meteorological Society*, *99*, 1177–1195. https://doi.org/10.1175/BAMS-D-16-0118.1

McRae, D. J., & Flannigan, M. D. (1990). Development of large vortices on prescribed fires. *Canadian Journal of Forest Research*, *20*(12), 1878–1887. https://doi.org/10.1139/x90-252

McRae, R. H. D., Sharples, J. J., & Fromm, M. (2015). Linking local wildfire dynamics to pyroCb development. *Natural Hazards and Earth System Sciences*, *15*(3), 417–428. https://doi.org/10.5194/nhess-15-417-2015

McRae, R. H., Sharples, J. J., Wilkes, S. R., & Walker, A. (2013). An Australian pyro-tornadogenesis event. *Natural Hazards*, *65*, 1801–1811. https://doi.org/10.1007/s11069-012-0443-7

Mitchell, R. M., O'Brien, D. M., & Campbell, S. K. (2006). Characteristics and radiative impact of the aerosol generated by the Canberra firestorm of January 2003. *Journal of Geophysical Research*, *111*, D02204. https://doi.org/10.1029/2005JD006304

Peace, M., McCaw, L., Santos, B., Kepert, J., Burrows, N., & Fawcett, R. J. B. (2017). Meteorological drivers of extreme fire behaviour during the Waroona bushfire, Western Australia, January 2016. *Journal of Southern Hemisphere Earth Systems Science*, *67*, 79–106. https://doi.org/10.22499/3.6702.002

Peterson, D., Campbell, J., Hyer, E., Fromm, M., Kablick, G., Cossuth, J., & DeLand, M. (2018). Wildfire-driven thunderstorms cause a volcano-like stratospheric injection of smoke. *NPJ Climate and Atmospheric Science*, *1*, 30. https://doi.org/10.1038/s41612-018-0039-3

Peterson, D., & Wang, J. (2013). A sub-pixel-based calculation of fire radiative power from MODIS observations: 2. Sensitivity analysis and potential fire weather application. *Remote Sensing of Environment*, *129*, 231–249. https://doi.org/10.1016/j.rse.2012.10.020

Peterson, D. A., Hyer, E. J., Campbell, J. R., Solbrig, J. E., & Fromm, M. D. (2017). A conceptual model for development of intense pyrocumulonimbus in western North America. *Monthly Weather Review*, *145*, 2235–2255. https://doi.org/10.1175/MWR-D-16-0232.1

Potter, B. E. (2012). Atmospheric interactions with wildland fire behaviour - II. Plume and vortex dynamics. *International Journal of Wildland Fire*, *21*(7), 802. https://doi.org/10.1071/wf11129

Potter, B. E., & Hernandez, J. R. (2017). Downdraft outflows: Climatological potential to influencefire behaviour. *International Journal of Wildland Fire*, *26*, 685–692. https://doi.org/10.1071/WF17035

Radeloff, V. C., Hammer, R. B., Stewart, S. I., Fried, J. S., Holcomb, S. S., & McKeefry, J. F. (2005). The wildland–urban interface in the United States. *Ecological Applications*, *15*(3), 799–805. https://doi.org/10.1890/04-1413

Rosenfeld, D., Fromm, M., Trentmann, J., Luderer, G., Andreae, M. O., & Servranckx, R. (2007). The Chisholm firestorm: Observed microstructure, precipitation and lightning activity of a pyro-cumulonimbus. *Atmospheric Chemistry and Physics*, *7*(3), 645–659. https://doi.org/10.5194/acp-7-645-2007

Rotunno, R., & Klemp, J. B. (1982). The influence of the shear-induced pressure gradient on thunderstorm motion. *Monthly Weather Review*, *110*(2), 136–151. https://doi.org/10.1175/1520-0493(1982)110<0136:TIOTSI>2.0.CO;2

Rudlosky, S. D., & Fuelberg, H. E. (2011). Seasonal, regional, and storm-scale variability of cloud-to-ground lightning characteristics in Florida. *Monthly Weather Review*, *139*(6), 1826–1843. https://doi.org/10.1175/2010MWR3585.1

Tedim, F., Leone, V., Amraoui, M., Bouillon, C., Coughlan, M., Delogu, G., et al. (2018). Defining extreme wildfire events: Difficulties, challenges, and impacts. *Firehouse*, *1*(1), 9. https://doi.org/10.3390/fire1010009

Tory, K. J., Thurston, W., & Kepert, J. D. (2018). Thermodynamics of pyrocumulus: A conceptual study. *Monthly Weather Review*, *146*(8), 2579–2598. https://doi.org/10.1175/MWR-D-17-0377.1

Thurston, W., Kepert, J. D., Tory, K. J., & Fawcett, R. J. B. (2017). The contribution of turbulent plume dynamics to long-range spotting. *International Journal of Wildland Fire*, *26*(4), 317. https://doi.org/10.1071/wf16142

Whittaker, J., & Taylor, M. (2018). *Community preparedness and responses to the 2017 New South Wales bushfires: Research for the New South Wales Rural Fire Service*. Melbourne: Bushfire and Natural Hazards CRC.

Williams, J. K., Cornman, L. B., Yee, J., Carson, S. G., Blackburn, G., & Craig, J. (2006). NEXRAD detection of hazardous turbulence. In *Proceedings of 44th AIAA aerospace sciences meeting and exhibit*, (pp. 2006–0076), Reno, NV, AIAA 2006-0076. [Available online at ftp://ftp.rap.ucar.edu/pub/jkwillia/NTDA/DAR_1/AIAA-2006-76-806.pdf.

Williams, J. K., & Meymaris, G. (2016). Remote turbulence detection using ground-based Doppler weather radar. In *Aviation Turbulence* (pp. 149–177). Basel, Switzerland: Springer International Publishing.